International Journal of Biological Macromolecules 347 (2026) 150609

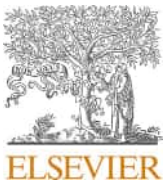

Contents lists available at ScienceDirect

International Journal of Biological Macromolecules

journal homepage: www.elsevier.com/locate/ijbiomac

Magnetic chitosan-based biosorbents for phosphorus removal from wastewater: Adsorption properties and mechanistic insights

H. William Myers [a], Bincheng Ma [b], Xianfei Wang [a], Dawei Li [a], Feihu Li [a,b,*]

[a] Collaborative Innovation Center of Atmospheric Environment and Equipment Technology, Jiangsu Key Laboratory of Atmospheric Environment Monitoring and Pollution Control, School of Environmental Science and Engineering, Nanjing University of Information Science and Technology, 219 Ningliu Road, Nanjing 210044, China

[b] NUIST Reading Academy, Nanjing University of Information Science and Technology, 219 Ningliu Road, Nanjing 210044, China

ARTICLE INFO

Keywords:
Phosphate removal
Magnetic biosorbent
Cerium carbonate hydroxide ($CeCO_3OH$)
Zirconium oxide (ZrO_2)
Adsorption

ABSTRACT

To address the critical challenge of phosphorus pollution in surface waters, this study develops two chitosan-based magnetic biosorbents (denoted as Ce@mCS and Zr@mCS) for the efficient removal of phosphorus from wastewater. The biocomposites were engineered to provide a sustainable and high-performance solution, circumventing the limitations of existing phosphorus removal strategies. The successful fabrication of the biocomposites, including the incorporation of magnetic components (Fe_3O_4) and dispersion of Ce/Zr active centers (i.e., $CeCO_3OH$, ZrO_2) with the chitosan scaffolds, was rigorously confirmed through SEM, XRD, XPS, FTIR, and zeta potential analyses. Batch adsorption experiments were carried out to optimize key parameters, yielding removal efficiencies of 88.3% for Ce@mCS and 85.7% for Zr@mCS ($C_0 = 25$ mg L^{-1}, dosage = 0.5 g L^{-1}, $T = 298$ K, $t = 8$ h). The adsorption isotherm data were best described by the Langmuir model, indicating monolayer adsorption with maximum capacities of 62.23 mg g^{-1} for Ce@mCS and 45.07 mg g^{-1} for Zr@mCS, respectively. Recycling performance analysis confirms the excellent capacity retention of both biocomposites over five consecutive cycles, validating their high practical potential promise. Post-adsorption characterization reveals that the mechanism for P capture lies in ligand exchange, Coulombic attraction, and H-bonding. This work exemplifies chitosan-based magnetic biocomposites for phosphate removal and underscores the promise of tailored biosorbents, providing a viable path for sustainable wastewater remediation and management.

1. Introduction

The excessive discharge of phosphate-containing wastewater into aquatic environments has become a significant global concern due to its role in eutrophication, which leads to harmful algal blooms, oxygen depletion, and ecosystem deterioration [1]. Phosphate (P), originating from various anthropogenic activities including agricultural runoff, industrial discharges, and domestic wastewater, must be effectively removed to maintain water quality and prevent environmental damage. Consequently, the development and implementation of efficient phosphate removal technologies are not merely a treatment objective but a critical imperative for safeguarding water resources and maintaining ecological equilibrium. Regulatory bodies worldwide have implemented strict phosphate discharge limits, requiring wastewater treatment plants to adopt advanced removal technologies [2].

Among various P removal methods, adsorption technology has emerged as a promising approach due to its high efficiency, operational simplicity, and potential for resource recovery [3,4]. While a plethora of adsorbents have been investigated, including metal oxides, layered double hydroxides, and polymeric materials, many suffer from intrinsic limitations that hinder their widespread practical application [5,6]. Furthermore, many reported materials exhibit insufficient adsorption capacity, slow kinetics, or a pronounced susceptibility to competing anions commonly present in complex wastewater matrices, such as chloride, sulfate, and bicarbonate [7]. Chitosan, a natural biopolymer derived from chitin, has garnered considerable attention as a sustainable biosorbent owing to its abundance, biocompatibility, biodegradability, and presence of functional groups that can be easily modified for

* Corresponding author at: Collaborative Innovation Center of Atmospheric Environment and Equipment Technology, Jiangsu Key Laboratory of Atmospheric Environment Monitoring and Pollution Control, School of Environmental Science and Engineering, Nanjing University of Information Science and Technology, 219 Ningliu Road, Nanjing 210044, China.
E-mail address: fhli@nuist.edu.cn (F. Li).

https://doi.org/10.1016/j.ijbiomac.2026.150609
Received 1 December 2025; Received in revised form 15 January 2026; Accepted 27 January 2026
Available online 28 January 2026

enhanced adsorption performance [8–11]. So far, a diverse array of chitosan-based biosorbents, whether in their native structure or cross-linked variations, have demonstrated effective phosphate removal and recovery [10,12–17]. Notably, modifications of chitosan with metal compounds, such as cerium (Ce), zirconium (Zr), iron (Fe), and lanthanum (La), have emerged as a versatile means to enhance its adsorption capacity and selectivity toward phosphate [8–10,17]. While these composite adsorbents exhibit high adsorption capacities and selectivity, a significant challenge lies in the separation and reclamation of these powdery adsorbents from treated water, which can be energy-intensive and costly, leading to losses in adsorbents during solid-liquid interactions [18,19]. To tackle these challenges, magnetic chitosan (mCS) composites incorporating magnetic particles like magnetite (Fe_3O_4) have emerged, offering excellent adsorption performance with straightforward recoverability through external magnetic assistance [8,19–22].

Recent studies underscore the efficacy of mCS for capturing P from wastewater. For instance, Wan and colleagues showed that Zr-loaded magnetic chitosan-polyvinyl alcohol hydrogel beads (Zr/Fe_3O_4/CS/PVA) with a maximum adsorption capacity of 50.76 mg g^{-1}, benefiting from advantageous mechanical properties through an interpenetrating polymer network [23]. More recently, a cerium carbonate hydroxide ($CeCO_3OH$)-decorated magnetic biosorbent has been demonstrated to have a remarkable capacity for phosphate (203.88 mg g^{-1}) [21]. To date, the exploration of more complex, nanostructured metal (oxy)hydroxides, such as cerium carbonate hydroxide, as functionalizing agents for magnetic chitosan remains a significantly underexplored frontier. Moreover, a direct comparative evaluation of different metal-based active sites (e.g., Ce vs. Zr) within an otherwise identical mCS scaffold is lacking, which is crucial for understanding structure-property relationships. To bridge these gaps, this study introduces two novel chitosan-based magnetic biosorbents, namely $CeCO_3OH$-loaded (Ce@mCS) and ZrO_2-loaded (Zr@mCS) magnetic chitosan composites, specifically designed for efficient phosphate removal from wastewater. The selection of $CeCO_3OH$ and ZrO_2 as functional materials is based on their strong affinity toward phosphate ions, excellent chemical stability, and environmental compatibility [21,24]. $CeCO_3OH$ possesses unique properties, including high surface reactivity and selective binding capability, while ZrO_2 exhibits exceptional stability across a wide pH range and strong ligand-binding properties [8]. The incorporation of magnetic Fe_3O_4 nanoparticles into the chitosan matrix enables rapid and efficient separation of the saturated adsorbents from treated water using external magnetic fields, addressing a critical challenge in practical applications. This comparative study of two distinct rare-earth and transition metal oxide-loaded chitosan composites provides valuable insights into structure-performance relationships and offers a systematic approach for optimizing adsorbent design for phosphate removal.

This study aims to: i) develop and characterize two novel magnetic chitosan composites for enhanced phosphate removal from wastewater; ii) systematically evaluate and compare the phosphate adsorption performance of Ce@mCS and Zr@mCS under diverse experimental conditions, including varying solution pH, initial phosphate concentration, contact time, temperatures, and presence of competing ions; and iii) elucidate the adsorption mechanisms through detailed analyses using spectroscopic techniques, surface characterization, and modeling of adsorption isotherms, kinetics, and iv) identify the optimal adsorbent and operating conditions for effective phosphate removal in various wastewater treatment scenarios. Through this comprehensive investigation, we aim to provide new insights into the design of high-performance chitosan-based biosorbents and contribute to the development of sustainable wastewater treatment technologies.

2. Materials and methods

2.1. Materials

Ferrous sulfate heptahydrate ($FeSO_4{\cdot}7H_2O$, $\geq$ 99.0%), sodium hydroxide (NaOH), and zirconium oxychloride octahydrate ($ZrOCl_2{\cdot}8H_2O$, 99.0%) were purchased from Sinopharm Chemical Reagent Co., Ltd. (Shanghai, China). Cerium (III) chloride heptahydrate ($CeCl_3{\cdot}7H_2O$, 99.0%) was obtained from Macklin Biochemical Co., Ltd. (Shanghai, China). Chitosan powder (molecular weight: 1526.5 g mol^{-1}) and ammonia solution (NH_4OH) were bought from Aladdin Biochemical Technology Co., Ltd. (Shanghai, China). Ferric nitrate nonahydrate ($Fe(NO_3)_3{\cdot}9H_2O$, 98.5%) and polyethylene glycol (PEG 8000) were obtained from Xilong Chemical Co., Ltd. (Guangzhou, China). Potassium dihydrogen phosphate (KH_2PO_4, 99.99%, Merck KGaA, Shanghai) was used to prepare the phosphate stock solution (1000 mg L^{-1}). Other chemicals are of analytical grade (AR) or above unless otherwise stated. All solutions were prepared using ultrapure deionized (DI) water (18.2 MΩ·cm, 25 °C).

2.2. Synthesis and characterization of magnetic biosorbents

The details of preparation of two magnetic biosorbents — $CeCO_3OH@Fe_3O_4$/Chitosan (denoted as Ce@mCS), and $ZrO_2@Fe_3O_4$/Chitosan (denoted as Zr@mCS) were specified in the Text S1-S5 (Supporting Information). Briefly, the pre-synthesized $CeCO_3OH$ particles and Fe_3O_4/Chitosan (denoted as Fe_3O_4/CS) are mixed and hydrothermally treated (50 °C, 12 h), yielding the Ce- or Ze-loaded biosorbents (Fig. 1a). The as-prepared magnetic biosorbents were then characterized thoroughly using a range of analytical techniques to assess their structural, surface, and compositional properties. Specifically, X-ray diffraction (XRD) analysis was conducted on an XRD-6000 diffractometer (Shimadzu, Japan) with Cu Kα radiation at a tube voltage of 40 kV and a tube current of 30 mA (step size: 0.02°, scanning rate: 5° min^{-1}). Fourier transform infrared (FTIR) spectroscopy was performed on a Nicolet iS50 infrared spectrometer (Thermo Fisher, USA) using the KBr pellet method [25]. Scanning electron microscopy (SEM) was employed to examine the morphological properties of both biosorbents on a Gemini 300 field emission scanning electron microscope (ZEISS, Germany). X-ray photoelectron spectroscopy (XPS) analysis was conducted on an electron spectrometer (UIVAC-PHI, Japan) using 300 W Al Kα radiation ($h\nu$ = 1486.6 eV), with the adventitious carbon (C 1s, 284.8 eV) for binding energy (BE) correction. Zeta (ζ) potentials of the as-prepared biosorbents were measured on a Zetasizer Nano ZS90 (Malvern, UK) under ambient conditions (25 °C, 1 atm) in solutions with varying pH over the range of 2–10.

2.3. Adsorption experiments

Unless otherwise specified, the adsorption tests were conducted in batch and on a Labquake tube rotator (Thermo Scientific, USA) with a speed of 80 rpm. The biosorbent dosage, experimental temperature, and initial pH of the solutions were maintained at 0.5 g L^{-1}, 25 °C, and 6.0 ± 0.1, respectively. After adsorption, the supernates were collected by centrifugation (8000 rpm for 15 min) and filtration with a 0.45 μm PES filter (Navigator, Tianjin) for phosphate measurement. The phosphate concentration was determined on an UV–vis spectrophotometer (UV-9200, Beijing Rayleigh Instrument Co., China) at 700 nm following the ascorbic acid method [26]. All experiments were performed in triplicate. The adsorption capacity of the biosorbent and the removal of phosphate under equilibrium conditions were obtained by the following equations (Eqs. 1, 2),

$$Q_e = \frac{(C_0 - C_e)V}{m} \quad (1)$$

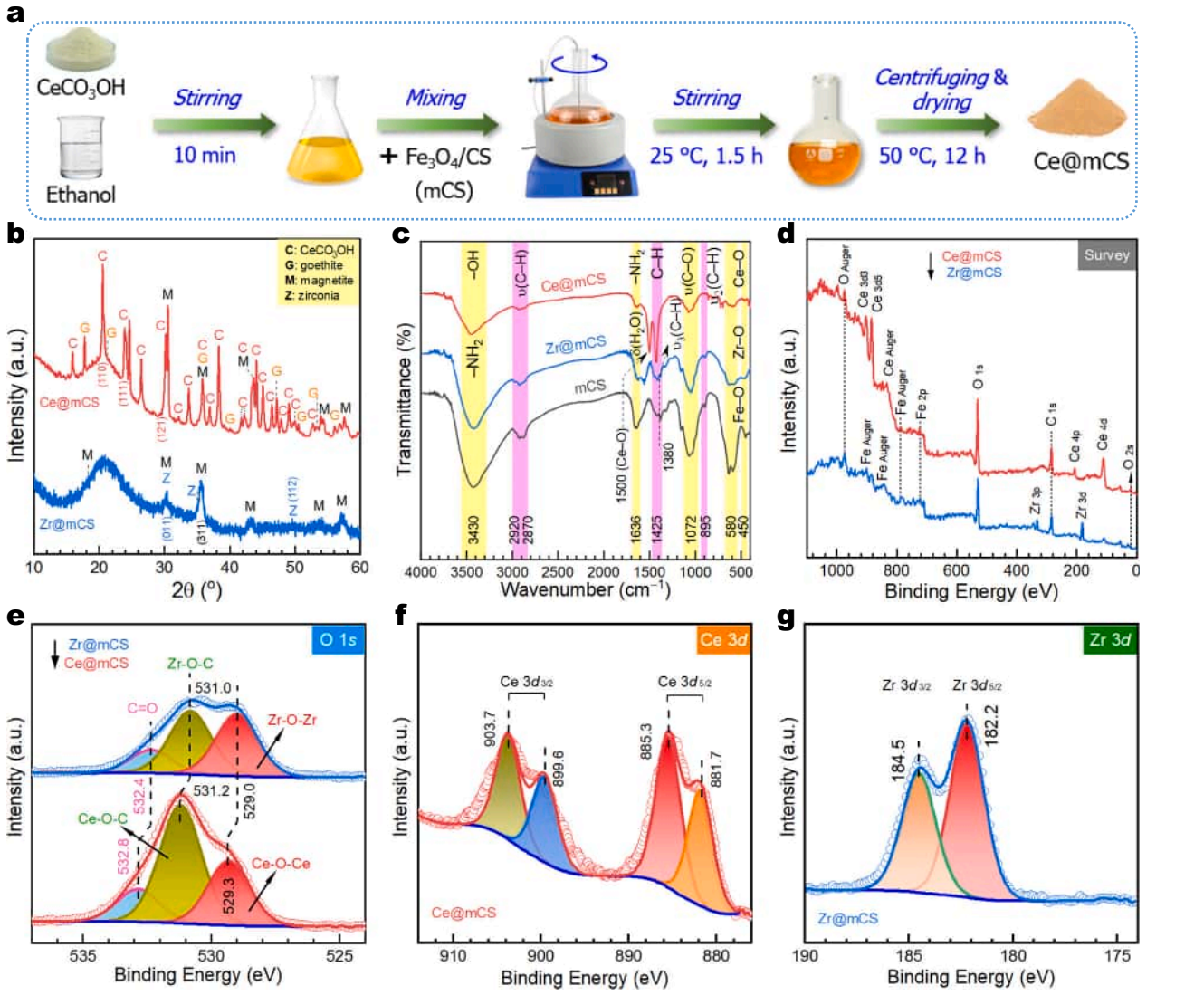

Fig. 1. (**a**) Schematic representation of the preparation of magnetic biosorbents (e.g., Ce@mCS); (**b-g**) Characterizations of the as-prepared magnetic biosorbents (i.e., Ce@mCS and Zr@mCS): (**b**) XRD patterns, (**c**) FTIR spectra, (**c**) survey XPS, (**e**) O 1s, (**f**) Ce 3d, and (**g**) Zr 3d regional XPS spectra.

$$R\% = \frac{C_0 - C_e}{C_0} \times 100\% \quad (2)$$

where C_0 and C_e (mg L^{-1}) are the initial and final concentration of phosphate in the aqueous solution, respectively, V refers to the volume of the solution (in L), and m is the mass of the biosorbent (in g).

To evaluate the effect of pH on P adsorption, the solution pH values were adjusted to 2–12 with 0.1 M HCl and NaOH, respectively, with an initial phosphate concentration (P-loading, C_0) of 30 mg PO_4^{3-} L^{-1}. The effect of P-loading on P adsorption was also examined over the range of 5–30 mg PO_4^{3-} L^{-1} at a constant pH of 6.0. To study the effect of co-existing species— Cl^-, SO_4^{2-}, NO_3^-, and humic acid (HA)—on phosphate adsorption, different amounts (10–30 mg L^{-1}) of such species were added to 100 mL of phosphate solution (C_0 = 10 mg PO_4^{3-} L^{-1}). After mixing for 24 h, the supernatant was filtered and analyzed, and the phosphate removal (%) was calculated. Following our earlier protocol [27], the adsorption kinetics were conducted with a P-loading of 30 mg PO_4^{3-} L^{-1} (pH = 6.0 ± 0.1) and a contact time ranging from 5 to 240 min. The experimental data were fitted with the pseudo-first-order (PFO, Eq. 3), pseudo-second-order (PSO, Eq. 4), and intraparticle diffusion (IPD, Eq. 5) models formulated below,

$$Q_t = Q_e\left(1 - e^{-k_1 t}\right) \quad (3)$$

$$\frac{t}{Q_t} = \frac{1}{k_2 Q_e^2} + \frac{t}{Q_e} \quad (4)$$

$$Q_t = k_p t^{1/2} + C \quad (5)$$

where Q_t and Q_e refer to the adsorption capacity (mg PO_4^{3-} L^{-1}) at contact time t (h) and equilibrium; k_1, k_2, and k_p stand for the pseudo-first, pseudo-second order, and IPD rate constants, respectively; C denotes a constant for any experiment in mg g^{-1}.

The adsorption isotherm experiments were performed with C_0 varying from 10 to 100 mg PO_4^{3-} L^{-1}, and a contact time of 24 h. The isotherm data were fitted with the Freundlich (Eq. 6), Langmuir (Eq. 7), and Temkin (Eq. 8) models shown as follows,

$$Q_e = k_F C_e^{1/n} \quad (6)$$

$$Q_e = \frac{k_L Q_m C_e}{1 + k_L C_e} \quad (7)$$

$$Q_e = \frac{RT}{b}\ln(k_T \bullet C_e) \quad (8)$$

where k_F (in (mg^{1-n} L^n) g^{-1}) and n denote the Friedrich constants, k_L refers to the Langmuir adsorption energy constant (L mg^{-1}), Q_m refers to the theoretical maximum adsorption capacity (mg PO_4^{3-} g^{-1}); R denotes the gas constant (8.314 J mol^{-1} K^{-1}), T is the temperature (K), k_T indicates the equilibrium binding constant (L mg^{-1}), and b denotes the Temkin constant related to the heat of adsorption (J mol^{-1}).

2.4. Regeneration and cycling test

Both the Ce@mCS and Zr@mCS biosorbents were chosen for the cycling test following the method specified elsewhere [28]. Briefly, after mixing and equilibrating in a phosphate solution ($C_0 = 20$ mg PO_4^{3-} L^{-1}) on a Labquake tube rotator for 8 h, the exhausted biosorbents were separated from the suspensions through centrifugation at 8000 rpm and rinsed with 10 mL of dilute NaOH (0.1 M). Then, the regenerated biosorbents were further rinsed with 40 mL of DI water and separated from the rinsing water via centrifugation for the next adsorption cycle. The cycling tests were performed at 25 °C for 10 successive cycles.

3. Results and discussion

3.1. Characterization of the as-prepared biosorbents

The XRD patterns depicted in Fig. 1b provide critical insight into the crystallographic structure and phase composition of the as-prepared magnetic biosorbents (i.e., Ce@mCS and Zr@mCS). The presence of distinct diffuse humps over the 2θ range of 15–30° along with the fluctuant baseline in both patterns is a characteristic signature of the inherent amorphous fractions of the chitosan matrix, which forms the foundational polymeric support for the inorganic components [9]. For the Ce@mCS composite, the XRD pattern reveals well-defined crystalline peaks at 2θ values of approximately 20.5°, 24°, 30°, and 35.8°, which are explicitly assigned to the (110), (111), and (121) lattice planes of $CeCO_3OH$ (JCPDS # 41–0013) and the (311) plane of magnetite, Fe_3O_4 (JCPDS # 75–0449) [20,29]. The coexistence of these distinct reflections, alongside other matching peaks, provides strong evidence for the successful integration of both cerium carbonate hydroxide and magnetite phases within the composite biosorbent. Notably, the detection of additional reflections corresponding to goethite (α-FeOOH, JCPDS # 29–0713) suggests a partial transformation of the magnetite phase, likely induced by the oxidative conditions of the hydrothermal treatment process [22]. In the Zr@mCS biosorbent, the diffraction pattern is dominated by magnetite reflections, but also features two broad and low-intensity peaks at 2θ ~ 30.2° and 50.4°, which are indexed to the (011) and (112) planes of zirconia (ZrO_2, JCPDS #50–1089) [30]. The considerable breadth and weak intensity of these zirconia-related peaks are indicative of a poorly crystalline or nanocrystalline ZrO_2 phase, confirming its successful loading onto the magnetic chitosan matrix. In addition to the XRD data, the FTIR spectra (Fig. 1c) illuminate the molecular vibrations and functional groups present in the biosorbents. The spectra exhibit a broad absorption band centered at 3430 cm^{-1}, which corresponds to the overlapping O–H and N–H stretching vibrations, while the band at 1636 cm^{-1} is attributed to their corresponding bending modes [31]. The characteristic aliphatic C–H stretching vibrations are evident from the bands at 2920 and 2870 cm^{-1}, with further confirmation from the bending, asymmetric stretching (ν_3(C–H)), and out-of-plane bending vibrations observed at 1425, 1380, and 895 cm^{-1}, respectively [30]. The symmetric stretching vibration of the C–O group is identified at 1072 cm^{-1}. Crucially, the presence of metal-oxygen bonds is confirmed by the appearance of bands at 1500 cm^{-1}, assigned to Ce–O stretching [21], and the lower frequency bands at 580 and 450 cm^{-1}, which are characteristic of Fe–O and other metal-oxygen vibrational modes (e.g., Ce–O, Zr–O) [27,30,31], thereby verifying the incorporation of the metallic species into the biosorbent frameworks.

XPS analysis was conducted to elucidate the surface elemental composition and chemical states of the as-prepared biosorbents (Fig. 1d-g). The survey spectra (Fig. 1d) confirm the presence of carbon, oxygen, and iron, along with distinct Ce and Zr signals in the Ce@mCS and Zr@mCS composites, respectively, providing direct evidence for the successful anchoring of the intended metal species onto the magnetic chitosan matrix. High-resolution regional scans further revealed the chemical environment of these elements, where the deconvolution of the O 1s spectra identified contributions from C=O, C–O, and metal-oxygen (M–O) bonds (Fig. 1e), confirming the integration of the inorganic phases within the organic polymer network. Importantly, the core-level spectra of Ce 3d and Zr 3d both exhibited pronounced spin-orbit splitting (Fig. 1f,g), which is a definitive signature of the +3 and + 4 oxidation state for cerium and zirconium, respectively, consistent with the presence of Ce(III) in $CeCO_3OH$ and Zr(IV) in ZrO_2. This is consistent with the above O 1s signal with strong M–O bonds, signifying a strong chemical interaction between the metal oxides and the chitosan substrate [19].

The morphological evolution of these materials observed via SEM (Fig. 2) corroborates these findings visually. While the pristine mCS consists of irregular, polydisperse particles with a rough surface ideal for nucleation (Fig. 2a), the functionalized composites (Fig. 2b,c) display significant agglomeration and an increase in particle size, which is a common phenomenon in composite materials, where the loading of inorganic phases fills the polymer's pores and bridges individual particles [32,33]. Notably, the surfaces of Ce@mCS and Zr@mCS are decorated with well-defined microcrystals, which are attributable to the anchored $CeCO_3OH$ and ZrO_2 phases [24]. Such surface decoration with metal oxide/hydroxide crystals on biopolymer templates has been frequently reported to create highly effective adsorbents; for instance, similar ZrO_2-chitosan composites have shown exceptional affinity for oxyanions like phosphate [8]. Therefore, the agglomeration and surface crystallization are not mere artifacts but are indicative of a successfully constructed architecture where the magnetic chitosan framework acts as a host for the microcrystals that serve as the core sites for phosphate capture through inner-sphere complexation [8,21].

3.2. Effects of P-loading and pH on phosphate adsorption

The adsorption efficiency of phosphate onto the as-prepared biosorbents, Ce@mCS and Zr@mCS, is profoundly influenced by P-loading and the solution pH (Fig. 3). P-loading acts as a critical driving force for adsorption kinetics and capacity [34]. At a fixed adsorbent dosage of 0.5 g L^{-1}, contact time of 2 h, and pH ~6.0, both biosorbents exhibited a distinct maximum adsorption efficiency at a P-loading of 10 mg L^{-1}, achieving removal efficiencies (R%) of 87.9% and 78.5% for Ce@mCS and Zr@mCS, respectively (Fig. 3a). A decrease in P-loading from 10 to 5 mg L^{-1} does not yield a higher removal efficiency, contrary to what might be expected. This phenomenon is likely attributable to a synergy of kinetic and thermodynamic constraints, given that phosphate adsorption remained in a non-equilibrium state after 2 h at an initial concentration of 30 mg L^{-1} (Fig. 4). Specifically, the attenuated concentration gradient at lower P-loadings reduces the driving force for mass transfer, thereby impeding the diffusion of phosphate ions toward the biosorbent surface within the designated contact time [34,35]. Consequently, the system may require a longer duration to reach equilibrium (> 2 h), and the observed removal efficiency within a fixed experimental time (i.e., 2 h) could represent a nonequilibrium state, resulting in an observed R% that is lower than theoretically expected based on equilibrium conditions. However, higher P-loadings (e.g., 20 and 30 mg L^{-1}) did not yield a proportionally higher removal efficiency at a fixed contact time of 2 h, which is due to the limited accessible binding sites of both biosorbents for phosphate uptake. This limitation highlights the critical interplay between P-loading, contact time, and the

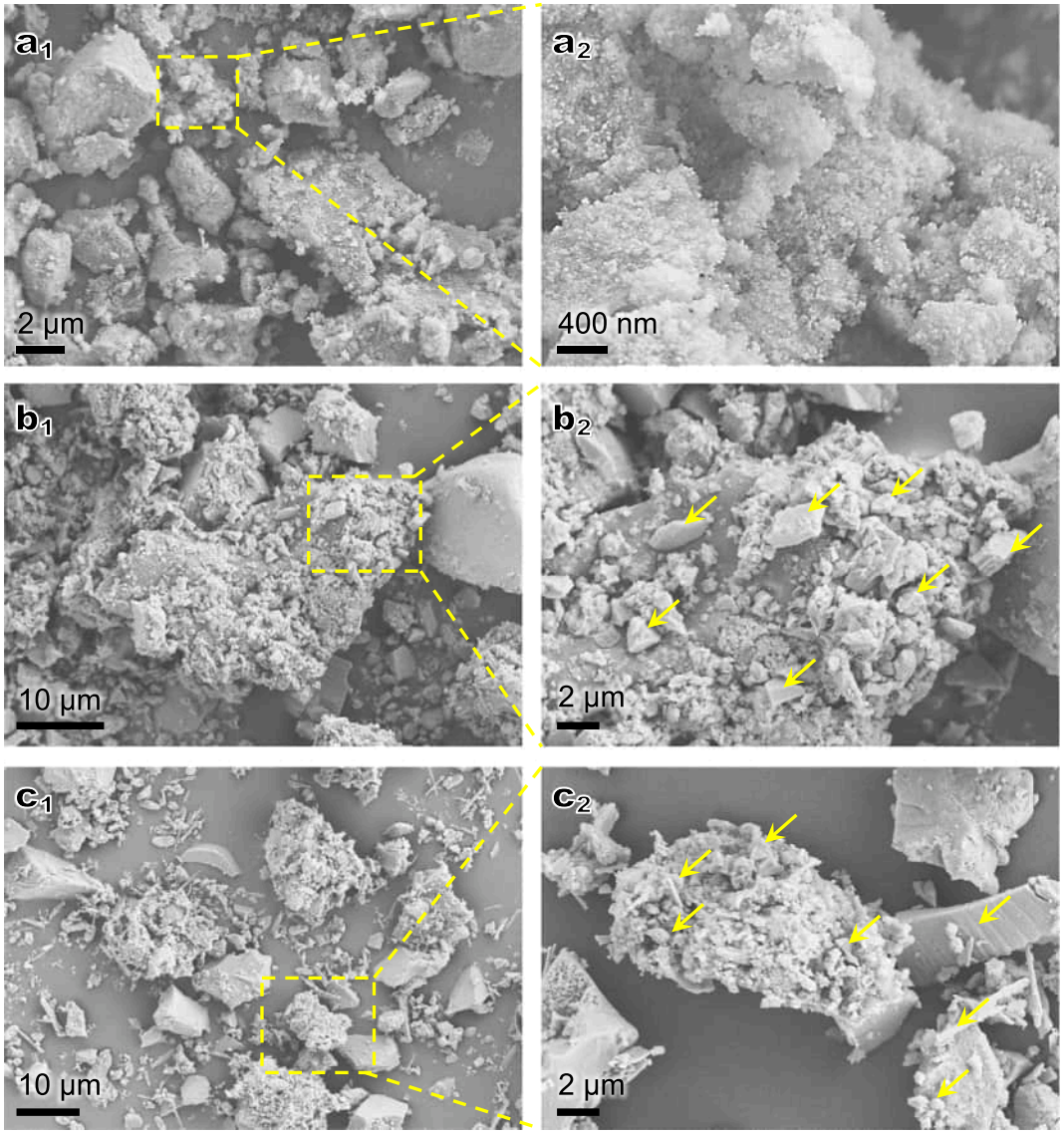

Fig. 2. SEM images of (**a**) Fe_3O_4/CS (i.e., mCS), (**b**) Ce@mCS, and (**c**) Zr@mCS. Note that there are well-defined crystals (highlighted by arrows) in both panels $\mathbf{b}_2$ and $\mathbf{c}_2$ after anchoring $CeCO_3OH$ and ZrO_2 over the mCS surfaces, indicative of successful anchoring of both metal (hydr)oxides onto the mCS matrix.

attainment of equilibrium conditions in batch adsorption experiments [8,34,35].

Beyond P-loading, the solution pH exerts a profound influence by modulating the surface charge of the biosorbents and the speciation of phosphate in the aqueous phase, creating a complex adsorption scenario (Fig. 3b-d). Zeta (ζ) potential measurements confirm that both Ce@mCS and Zr@mCS maintain a positive surface charge across a wide pH range (2−10) (Fig. 3b), favorable for attracting anionic phosphate species via a Coulombic attraction [20,21]. The pH-dependent adsorption profile (Fig. 3c,d), which increases with the solution pH to a maximum at pH ~6 before declining under alkaline conditions, can be deconstructed by examining electrostatic interactions and phosphate speciation. Specifically, at the optimal pH of 6, the combination of a substantial positive zeta potential of both biosorbents (~20 mV, Fig. 3b) and the predominance of monovalent $H_2PO_4^-$ (92.3%) creates an ideal scenario for strong Coulombic attractions between phosphate and the biosorbents. At pH above 6, while the biosorbents remain positively charged throughout the tested range, the increasing concentration of competing hydroxyl ions (OH^-) at higher pH regions progressively hinders phosphate access to binding sites through both electrostatic competition and specific ligand exchange [36]. The nearly identical zeta potentials and adsorption profiles for both biosorbents at this pH suggest a common, overarching mechanism dominated by Coulombic attraction. Nevertheless, the intrinsic affinity of cerium (Ce) and zirconium (Zr) for phosphate anions is well-established, often leading to the formation of stable inner-sphere complexes that enhance adsorption capacity beyond purely physical expectations [8,21]. Therefore, the high performance of these biosorbents toward P is likely due to a synergistic mechanism combining robust electrostatic attraction with specific, high-affinity chemical bonding at the metal oxide centers. Given the consistently excellent P adsorption performance observed in both Ce@mCS and Zr@mCS at pH ~6 across the tested P-loadings, this pH condition was selected as the optimal operating pH for all subsequent experiments.

3.3. Effect of coexisting species

The presence of diverse anions and organic compounds in natural waters necessitates evaluation of their influence on phosphate uptake by biosorbents, as phosphate is often the minority solute relative to these coexisting species [27,31,37]. In this regard, we comprehensively evaluated the impact of common aqueous interferents—chloride (Cl^-), bicarbonate (HCO_3^-), sulfate (SO_4^{2-}), and humic acid (HA)—on the

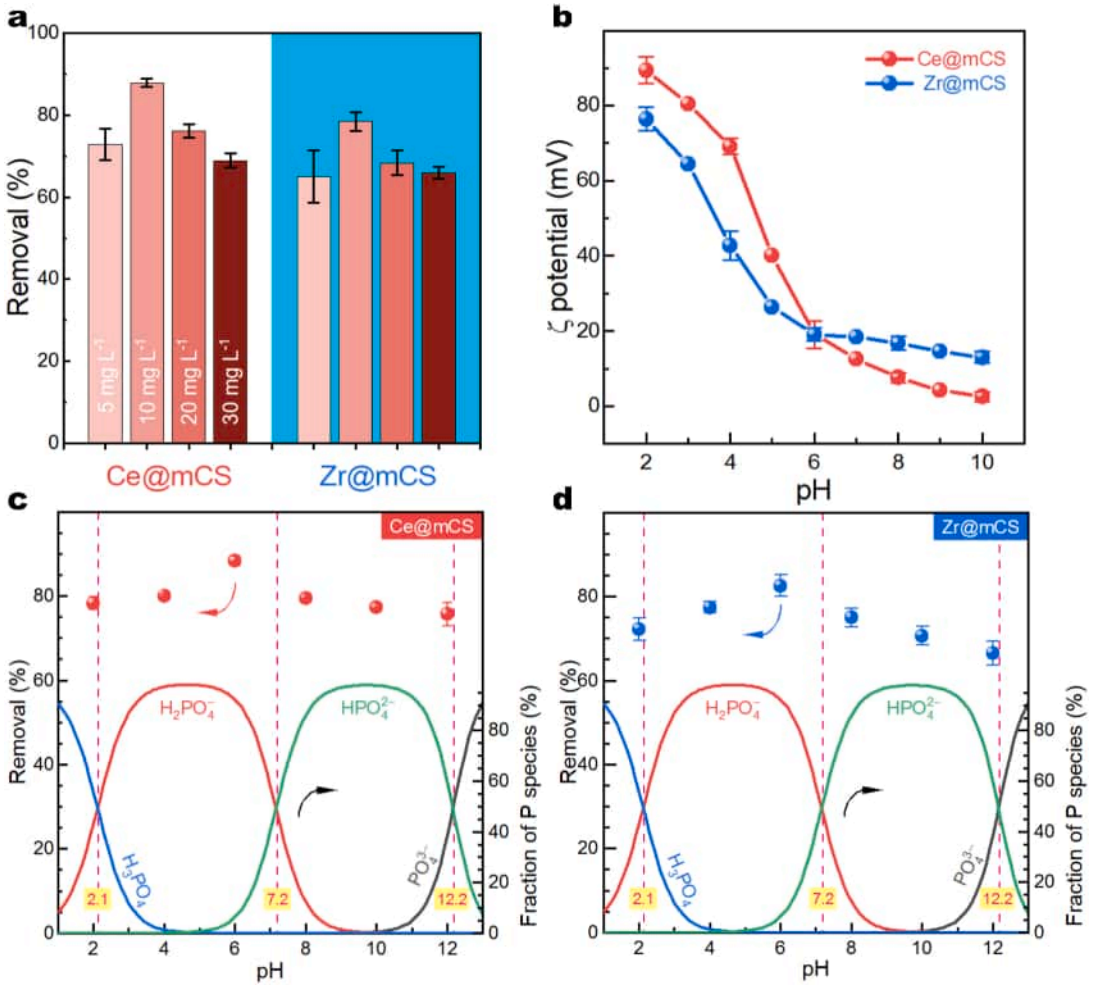

Fig. 3. (**a**) Effects of initial phosphate (PO_4^{3-}) concentration (C_0) on P adsorption onto Ce@mCS and Zr@mCS (pH = 6.0 ± 0.1, biosorbent dosage = 0.5 g L^{-1}, T = 298 K, contact time = 2 h); (**b**) ζ potentials of the as-prepared magnetic adsorbents in P-free solution with varying pH; (**c-d**) effects of pH on P adsorption onto (**c**) Ce@mCS, and (**d**) Zr@mCS (C_0 = 30 mg PO_4^{3-} L^{-1}, biosorbent dosage = 0.5 g L^{-1}, T = 298 K). Note that the speciation diagram of phosphate (7.35×10^{-4} mol L^{-1} of KH_2PO_4 solution at 298 K) in panels **c** and **d** was calculated using the Visual MINTEQ 3.1 software.

sequestration efficiency of the Ce@mCS and Zr@mCS biosorbents at an initial P-loading of 10 mg L^{-1}. As shown in Fig. S1a,b (Supporting Information), competing ions exerted varying degrees of inhibition on P adsorption across their respective concentrations. Anions such as Cl^- and HCO_3^- exhibited a negligible inhibitory effect on phosphate uptake, particularly at environmentally relevant lower concentrations. This minimal interference is a direct consequence of their weak competitive affinity, stemming from their monovalent nature and lower charge density, which diminishes their interaction with the biosorbents primarily to non-specific, outer-sphere electrostatic attraction [38]. These non-specific interactions are easily outcompeted by phosphate, which possesses a significantly higher intrinsic affinity for the binding sites, allowing for high removal efficiency to be maintained even in the presence of these background electrolytes.

In contrast, the divalent SO_4^{2-} demonstrated significant competition, leading to a substantial reduction in phosphate removal efficiency (Fig. S1a,b). The pronounced inhibitory effect of SO_4^{2-} is mechanistically rooted in its high charge density and its ability to engage in specific, inner-sphere complexation via ligand exchange [39], directly contesting for the metal-active centers (Zr/Ce) on the biosorbent surface. Additionally, the similar ionic radii (2.3 Å versus 2.38 Å for sulfate and phosphate, respectively) and tetrahedral geometries of sulfate and phosphate further intensify this competition for the same binding sites [40]. The robustness of the sulfate-biosorbent interaction is further underscored by its relatively high electron-pair donation capacity, facilitating the formation of stable complexes that effectively block phosphate access [41].

Beyond inorganic anions, the presence of HA, a prevalent component of natural organic matter in various aquatic environments, also impaired phosphate adsorption significantly [42,43]. The large, polyfunctional HA molecules usually adsorb onto the biosorbent surface, likely through electrostatic and complexation interactions, thereby increasing surface negativity and sterically hindering phosphate approach [44,45]. Despite these multifaceted competitive challenges, the biosorbents, particularly Zr@mCS, demonstrated remarkable resilience, maintaining a high phosphate removal efficiency of 73.1% even in the presence of a high HA concentration (30 mg L^{-1}, Fig. S1a,b). This robust performance underscores a degree of innate selectivity for phosphate and highlights the potential utility of these biosorbents in treating complex wastewater and natural waters where multi-component competition is the norm rather than the exception. Although the phosphate removal efficiencies of the biosorbents were decreased by 33.2% and 10.1%, respectively (Fig. S1c), due to the intense competition from coexisting species, particularly the DOMs in the real wastewater (RWW, Table S1). Their realistic effectiveness was further exemplified by the fact that both biosorbents maintained a relatively high removal efficiency toward phosphate (i.e., 59.2% and 74.5% for Ce@mCS and Zr@mCS, respectively) in the real wastewater sample.

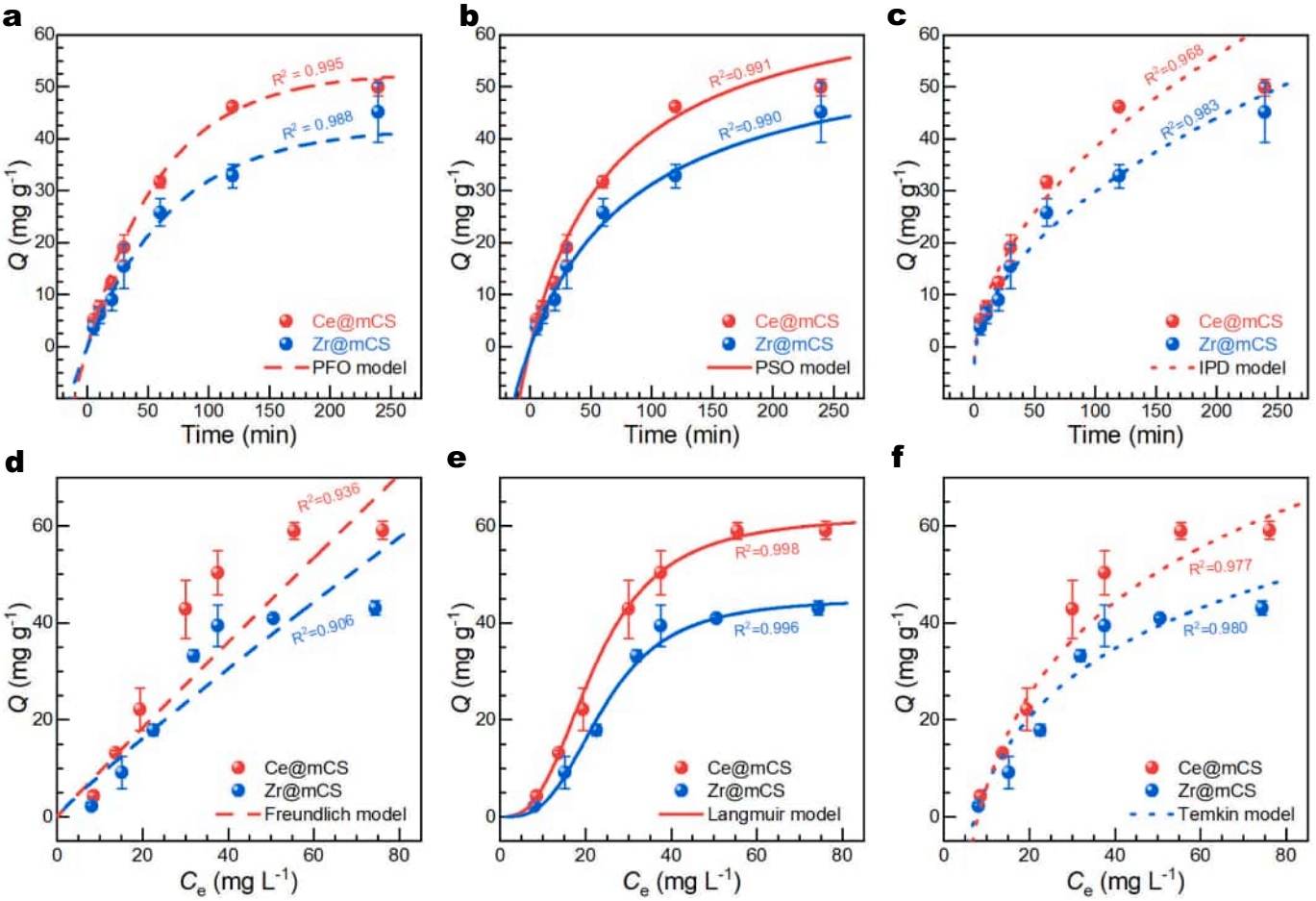

Fig. 4. (**a-c**) Adsorption kinetics and model fitting with (**a**) the pseudo-first-order (PFO), (**b**) the pseudo-second-order (PSO), and (**c**) the intraparticle diffusion (IPD) models (C_0 = 30 mg PO_4^{3-} L^{-1}, biosorbent dosage = 0.5 g L^{-1}, T = 298 K); (**d-f**) adsorption isotherms and model fitting with (**d**) the Freundlich, (**e**) the Langmuir, and (**f**) the Temkin models (C_0 = 10–100 mg PO_4^{3-} L^{-1}, biosorbent dosage = 0.5 g L^{-1}, T = 298 K, contact time = 24 h).

3.4. Adsorption kinetics

The kinetics profiles and modeling of P adsorption onto both biosorbents are presented in Fig. 4a-c. Initial rapid adsorption was observed during the first 1 h for both biosorbents, which is attributed to the plentiful accessible binding sites on the biosorbent surfaces, facilitating swift interactions with the dominant $H_2PO_4^-$ species in the solution (Fig. 3c) [46]. However, as time progressed, this adsorption rate gradually diminished as the active binding sites became saturated, culminating in a state of equilibrium after approximately 4 h. To explore the potential mechanisms behind P adsorption, three kinetic models, namely the pseudo-first-order (PFO), pseudo-second-order (PSO), and intraparticle diffusion (IPD) models, were employed to fit the adsorption kinetics data (Fig. 4a-c, Table S2). All these kinetic models can describe the kinetics data well, with high correlation coefficients (R^2) above 0.96 (Table S2). Comparatively, the PSO model yielded higher R^2 values (0.991 for Ce@mCS and 0.990 for Zr@mCS) than both the PFO (0.995, 0.988) and IPD models (0.968, 0.983), indicating that the PSO model is slightly better at predicting the adsorption kinetics behavior than other models. Note that the calculated equilibrium capacity value at presumed equilibrium state ($Q_{e,cal}$) from the PSO model closely matched the observed value ($Q_{e,exp}$) (Table S2), indicating that P adsorption on these biosorbents primarily occurs via a chemisorption process, this involves chemical bonding between the phosphate ions and the biosorbent surface, often resulting in a stable binuclear bond configuration [47].

Notably, both the Ce@mCS and Zr@mCS biosorbents are featured by hierarchical morphology (Fig. 2), which appears to facilitate P adsorption via a multiple-stage manner [27]. In general, P adsorption onto hierarchical adsorbents follows an order of initial rapid adsorption occurring at the external surface, gradual adsorption (diffusion-controlled), and equilibrium adsorption (forming inner-sphere complexation) [27]. The high R^2 values obtained from the IPD model indicate that P adsorption onto both biosorbents is dominated by the diffusion-controlled stage in the time frame. A higher C value was observed in Ce@mCS than that of Zr@mCS (Table S2), indicative of less intraparticle diffusion barriers and thereby higher P adsorption performance in Ce@mCS relative to Zr@mCS.

3.5. Adsorption isotherms

Although kinetic studies indicated that adsorption equilibrium was approximately achieved within 4 h (Fig. 4a), the isotherm experiments were deliberately extended to 24 h to unequivocally ensure saturation was complete across all concentration levels (10–100 mg PO_4^{3-} L^{-1}). As shown in Fig. 4d-f, P adsorption onto both biosorbents was initially rapid before plateauing as the systems approached equilibrium. This characteristic L-shaped profile is attributed to the rapid occupation of readily available binding sites on the biosorbent surfaces during the initial phase, indicative of a high affinity of both biosorbents for phosphate [27]. As adsorption proceeded, the progression toward equilibrium was governed by increasing competition among phosphate ions for a diminishing number of vacant active sites, an effect that became more pronounced at higher concentrations.

The equilibrium adsorption data were analyzed using the Freundlich, Langmuir, and Temkin isotherm models to elucidate the underlying mechanisms of the Ce@mCS and Zr@mCS materials. The Langmuir model demonstrated an exceptional fit to the experimental data, as indicated by a high correlation coefficient ($R^2 > 0.99$, Fig. 4e). This strong correlation suggests that adsorption occurs primarily via monolayer coverage on a homogeneous surface featuring sites of uniform energy [48]. The model yielded a maximum phosphate uptake capacity (Q_m) of 62.23 and 45.07 mg PO_4^{3-} g^{-1} for Ce@mCS and Zr@mCS, respectively (Table S3), which is indicative of a chemisorption process likely involving the formation of inner-sphere complexes between phosphate ions and the active Ce or Zr centers. In contrast, the Freundlich model, which describes multilayer adsorption on heterogeneous surfaces, provided a poor fit ($R^2 = 0.936$, and 0.906 for Ce@mCS and Zr@mCS, respectively, Fig. 4d). Note that the values of heterogeneity parameter ($1/n$) are less than 1 for both biosorbents, indicating that P adsorption over both biosorbents are a thermodynamically favorable process [25]. The Temkin isotherm, which accounts for adsorbate-adsorbate interactions and a linear decrease in adsorption heat with coverage, also correlated well with the experimental data ($R^2 = 0.977$, and 0.980 for Ce@mCS and Zr@mCS, respectively, Fig. 4f). The derived constants (k_T, and b, Table S3) signify a moderate adsorbent-adsorbate affinity and a relatively uniform distribution of binding energies across the surface, consistent with the Langmuir model's implications [49].

The comparative analysis reveals that Ce@mCS, with its capacity of 62.23 mg g^{-1}, ranks among the top-tier and competitive magnetic biosorbents for efficient phosphate removal under similar conditions (e.g., comparable P loading, Table S4). It shows comparable capacity to biomaterials such as ZrO_2-NaMMT composite (64.57 mg g^{-1}), Ce(IV)@CS (71.6 mg g^{-1}), and demonstrates a significant advantage over others like CS-CBC@Zr (31.89 mg g^{-1}) (Fig. 5a). The competitive performance of Ce@mCS can be attributed to its specific structural design and its rich surface chemistry. Specifically, the presence of amine (–NH_2), hydroxyl (–OH), and carboxyl (–COOH) functional groups provides multiple pathways for phosphate binding (Fig. 1c), potentially through hydrogen bonding and electrostatic attraction, which complement the primary chemisorption with metal ions [50]. This multifunctional nature, combined with a high specific capacity and the ease of magnetic separation, positions Ce@mCS as a highly promising and competitive biosorbent for phosphate remediation in aqueous systems.

3.6. Recycling performance

Recyclability and reusability are paramount for assessing the long-term cost-effectiveness and practical potential of biosorbents in industrial applications. The inherent magnetism of the Ce@mCS and Zr@mCS composites facilitates their rapid and easy separation from aqueous suspensions post-adsorption (inset of Fig. 5b), a critical feature for operational efficiency [20,28]. Over ten consecutive adsorption-desorption cycles, both biosorbents exhibited a near-linear decline in phosphate removal efficiency (Fig. 5b,c). The adsorption percentage for Ce@mCS decreased from 88.3% to 41.9%, while Zr@mCS dropped from 85.7% to 38.4%. This pattern of gradual capacity loss is consistent with observations from other studies using alkaline eluents for pollutant desorption [28]. The diminishing efficacy is likely due to the progressive and irreversible leaching of key functional groups from the biosorbent surface. Specifically, the loss of metal-hydroxyl complexes (Ce–OH, Fe–OH, Zr–OH) during the alkaline rinsing step impairs the primary mechanisms of phosphate uptake, namely ligand exchange and electrostatic interactions [27,31]. This leaching occurs during the desorption process itself, which employs a dilute NaOH solution for regeneration. Further comparative analysis indicates that both the Ce@mBC and Zr@mBC demonstrated excellent capacity retention over the initial five consecutive cycles (i.e., 81.9% and 72.5% for Ce@mBC and Zr@mBC, respectively), outperforming other Ce/Zr-based adsorbents under similar conditions (Fig. S2). This explicitly underscores the relative stability and distinct reusability profile of both biosorbents, signifying their high practical potential for scaling up to treat phosphate-contaminated wastewater.

3.7. Adsorption mechanism

To explore the underlying mechanisms for P adsorption, post-adsorption characterizations (XRD, FTIR, and XPS) of the P-loaded biosorbents after 10 circulative adsorption-desorption runs were performed and compared to those of the pristine biosorbents in Figs. 6, and S3–5. Note that the 2θ positions of the XRD pattern of the P-loaded Ce@mCS remain essentially unchanged upon P adsorption, with a slight decrease in peak intensity (Fig. 6a), indicating the phase integrity of the anchored $CeCO_3OH$ crystals. The recession in peak intensity is due to partial loss of these crystals during the desorption process, as evidenced by the removal efficiency descending during the repeated adsorption-desorption tests (Fig. 5b). Similar observations in biosorbent Zr@mCS also confirm this speculation (Fig. S3a).

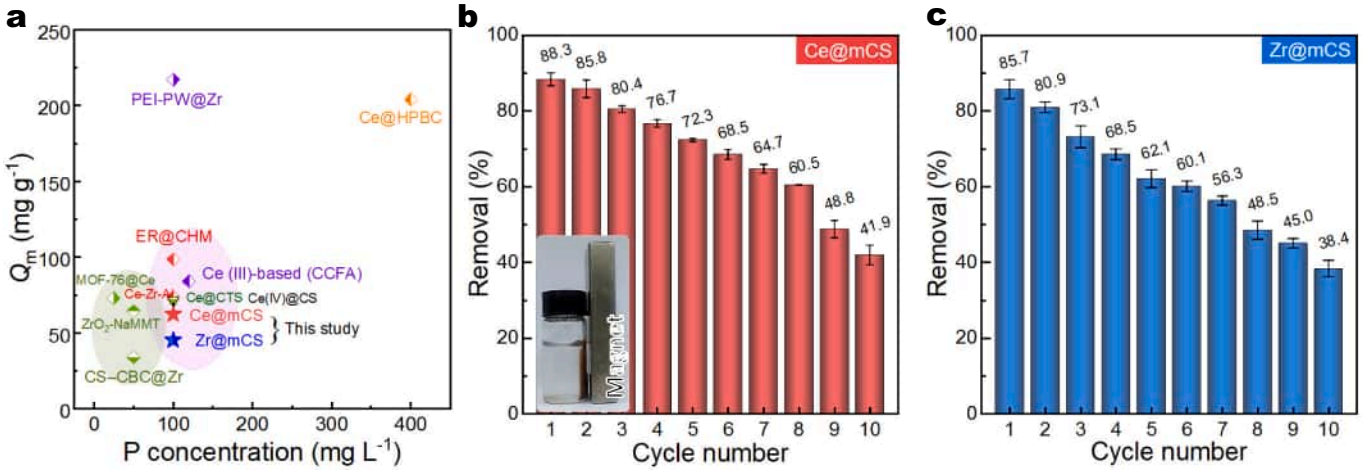

Fig. 5. (**a**) Comparison of adsorption capacity of both biosorbents with those from literature (data shown in Table S4); (**b-c**) the cycling performance of (**b**) Ce@mCS and (**c**) Zr@mCS for 10 successive adsorption-desorption cycles (C_o = 25 mg PO_4^{3-} L^{-1}, biosorbent dosage = 0.5 g L^{-1}, T = 298 K, contact time = 8 h, desorption eluent = 0.1 M of NaOH). The inset in panel **b** is the magnetic separation photograph of the biosorbents after adsorption.

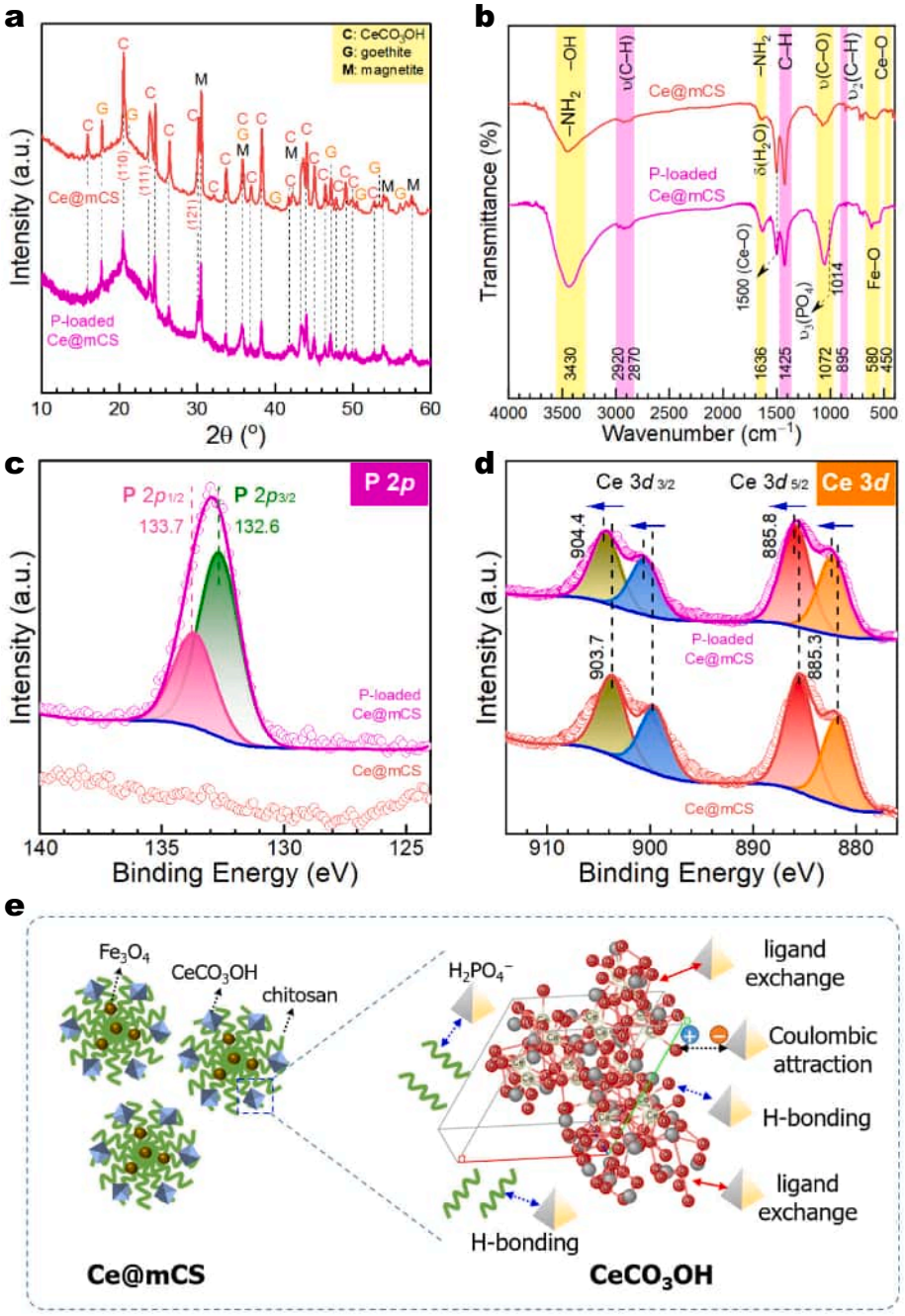

Fig. 6. Post-adsorption characterizations and possible mechanisms for P adsorption onto Ce@mCS: (**a**) XRD patterns, (**b**) FTIR, (**c**) P 2p, (**d**) Ce 3d regional XPS spectra of Ce@mCS biosorbent before and after P adsorption; and (**e**) the proposed adsorption mechanism illustration.

Complementary FTIR analysis provides further mechanistic validation (Figs. 6b, S3b). Specifically, a new infrared band assignable to the asymmetric stretching of phosphate ($\nu_3(PO_4)$, 1014 cm^{-1}) arose upon P adsorption, confirming the binding of phosphate onto the surface of these biosorbents [27]. Besides, the strength of the $-NH_2$ band at 1636 cm^{-1} increased slightly upon P adsorption, implying this group is likely involved in P adsorption via H-bonding [50]. This is further corroborated by XPS analysis of the P-loaded biosorbents — the emergence of P 2p peaks in both the survey and P 2p regional XPS spectra (Figs. 6c, S4–5). Additionally, deconvolution analysis of regional O 1sspectra reveals that phosphate is primarily bound with metal hydroxyl via ligand exchange (i.e., $H_2PO_4^-$ + >Ce-OH → >Ce-O-PO_3H_2 + OH^-, $H_2PO_4^-$ + >Zr-OH → >Zr-O-PO_3H_2 + OH^-), forming robust Ce–O–P or Zr−O−P bonds (Figs. S4b, S5b). Evidence for this mechanism is provided by a clear blue-shift (shift toward higher binding energy) in the Ce 3d and Zr 3d XPS spectra (Figs. 6d, S5d), reflecting electron density redistribution as phosphate replaces weaker ligands on these active sites [27,31,51]. These spectroscopic signatures collectively underscore a concerted adsorption process involving ligand exchange at Ce/Zr sites and secondary interactions with organic functional groups, aligning with established mechanisms for phosphate sequestration on metal oxides [21,26].

Apart from the ligand exchange mechanism, Coulombic attraction facilitated by the biosorbent's positive surface charge (ζ ~ 20 mV at pH 6, Fig. 3b) would enhance the migration of negatively charged phosphate species (i.e., $H_2PO_4^-$) to these active sites, boosting P uptake by

electrostatic adsorption. As mentioned above, the chitosan matrix possesses a variety of functional groups, which can also contribute to P sequestration via H-bonding, electrostatic attractions [50]. Collectively, the potential mechanisms for P adsorption are i) ligand exchange (inner-sphere complexation), ii) Coulombic attraction, and iii) H-bonding (Fig. 6e). Future studies based on density functional theory (DFT) calculations, and in situ spectroscopy (e.g., attenuated total reflection Fourier transform infrared, ATR-FTIR) may be needed for more in-depth mechanistic insights of phosphate adsorption onto such biosorbents. From a practical perspective, further pilot-scale testing would be required to validate the long-term performance of both biosorbents in continuous-flow systems, particularly for treating real wastewater matrices.

4. Conclusion

In summary, two chitosan-based magnetic biosorbents anchored with $CeCO_3OH$ and ZrO_2 have been prepared via a step-wise manner. The as-prepared biosorbents (i.e., Ce@mCS and Zr@mCS) demonstrated high efficiency in phosphate uptake from aqueous solutions. Batch adsorption results revealed that P adsorption onto both biosorbents is pH-dependent, with the maximum adsorption performance occurring at pH 6. Kinetic analysis indicated a pseudo-second-order adsorption process for P adsorption onto both biosorbents, suggesting chemisorption mechanisms. The adsorption isothermal data aligned well with the Langmuir model, signifying maximum adsorption capacities of 62.23 and 45.07 mg PO_4^{3-} g^{-1} for Ce@mCS and Zr@mCS, respectively, which is competitive to the state-of-the-art biosorbents for P uptake. Notably, both biosorbents demonstrated excellent capacity retention over the initial five consecutive cycles, and a relatively high removal efficiency toward phosphate in real wastewater samples rich in competitive species, validating their high practical potential. Mechanistic analysis indicates that phosphate appears to be sequestered via i) ligand exchange (inner-sphere complexation), ii) Coulombic attraction, and iii) H-bonding. These findings collectively highlight the practical potential of Ce@mCS and Zr@mCS as cost-effective biosorbents for phosphate removal, offering a promising solution for phosphate-contaminated wastewater remediation.

CRediT authorship contribution statement

H. William Myers: Writing – original draft, Visualization, Methodology, Investigation. **Bincheng Ma:** Validation, Investigation. **Xianfei Wang:** Visualization, Investigation. **Dawei Li:** Investigation. **Feihu Li:** Writing – review & editing, Writing – original draft, Visualization, Supervision, Conceptualization.

Declaration of competing interest

The authors declare that they have no known competing financial interests or personal relationships that could have appeared to influence the work reported in this paper.

Acknowledgments

This work is partially supported by the Priority Academic Program Development (PAPD) of Jiangsu Higher Education Institutions and the Innovation Training Programme for Undergraduate Students of NUIST (XJDC202510300570).

Appendix A. Supplementary data

Supplementary data to this article can be found online at https://doi.org/10.1016/j.ijbiomac.2026.150609.

Data availability

Data will be made available on request.

References

[1] D.J. Conley, H.W. Paerl, R.W. Howarth, D.F. Boesch, S.P. Seitzinger, K.E. Havens, C. Lancelot, G.E. Likens, Controlling eutrophication: nitrogen and phosphorus, Science 323 (2009) 1014–1015, https://doi.org/10.1126/science.1167755.
[2] J.J. Elser, D.F. Call, J.A. Deaver, O.W. Duckworth, B.K. Mayer, E. Mclamore, B. Rittmann, M. Mahmood, P. Westerhoff, The phosphorus challenge: biotechnology approaches for a sustainable phosphorus system, Curr. Opin. Biotechnol. 90 (2024) 103197, https://doi.org/10.1016/j.copbio.2024.103197.
[3] R.T. Liu, L.N. Chi, X.Z. Wang, Y.M. Sui, Y. Wang, H. Arandiyan, Review of metal (hydr)oxide and other adsorptive materials for phosphate removal from water, J. Environ. Chem. Eng. 6 (2018) 5269–5286, https://doi.org/10.1016/j.jece.2018.08.008.
[4] R. Altaf, B. Sun, H.J. Lu, H.P. Zhao, D.Z. Liu, Removal and recovery of phosphonates from wastewater via adsorption, Crit. Rev. Environ. Sci. Technol. 53 (2023) 1032–1058, https://doi.org/10.1080/10643389.2022.2115271.
[5] D. Luo, L.Y. Wang, H.Y. Nan, Y.J. Cao, H. Wang, T.V. Kumar, C.Q. Wang, Phosphorus adsorption by functionalized biochar: a review, Environ. Chem. Lett. 21 (2023) 497–524, https://doi.org/10.1007/s10311-022-01519-5.
[6] L.A. Wendling, P. Blomberg, T. Sarlin, O. Priha, M. Arnold, Phosphorus sorption and recovery using mineral-based materials: Sorption mechanisms and potential phytoavailability, Appl. Geochem. 37 (2013) 157–169, https://doi.org/10.1016/j.apgeochem.2013.07.016.
[7] M. Du, Y.Y. Zhang, Z.Y. Wang, M.R. Lv, A.Q. Tang, Y. Yu, X. Qu, Z.Q. Chen, Q. X. Wen, A. Li, Insight into the synthesis and adsorption mechanism of adsorbents for efficient phosphate removal: Exploration from synthesis to modification, Chem. Eng. J. 442 (2022) 136147, https://doi.org/10.1016/j.cej.2022.136147.
[8] H.L. Jiang, P.H. Chen, S.L. Luo, X.M. Tu, Q. Cao, M. Shu, Synthesis of novel nanocomposite Fe_3O_4/ZrO_2/chitosan and its application for removal of nitrate and phosphate, Appl. Surf. Sci. 284 (2013) 942–949, https://doi.org/10.1016/j.apsusc.2013.04.013.
[9] I.A. Kumar, C. Jeyaprabha, S. Meenakshi, N. Viswanathan, Hydrothermal encapsulation of lanthanum oxide derived Aegle marmelos admixed chitosan bead system for nitrate and phosphate retention, Int. J. Biol. Macromol. 130 (2019) 527–535, https://doi.org/10.1016/j.ijbiomac.2019.02.106.
[10] L. Wujcicki, T. Mandok, W. Budzinska-Lipka, K. Pawlusinska, N. Szozda, G. Dudek, K. Piotrowski, R. Turczyn, M. Krzywiecki, A. Kazek-Kesik, J. Kluczka, Cerium(IV) chitosan-based hydrogel composite for efficient adsorptive removal of phosphates (V) from aqueous solutions, Sci. Rep. 13 (2023) 13049, https://doi.org/10.1038/s41598-023-40064-1.
[11] Y.L. Zheng, Y.S. Wan, Y. Zhang, J.S. Huang, Y.C. Yang, D.C.W. Tsang, H.L. Wang, H. Chen, B. Gao, Recovery of phosphorus from wastewater: A review based on current phosphorous removal technologies, Crit. Rev. Environ. Sci. Technol. 53 (2023) 1148–1172, https://doi.org/10.1080/10643389.2022.2128194.
[12] J. Jang, D.S. Lee, Effective phosphorus removal using chitosan/Ca-organically modified montmorillonite beads in batch and fixed-bed column studies, J. Hazard. Mater. 375 (2019) 9–18, https://doi.org/10.1016/j.jhazmat.2019.04.070.
[13] J. Dai, H. Yang, H. Yan, Y.G. Shangguan, Q.A. Zheng, R.S. Cheng, Phosphate adsorption from aqueous solutions by disused adsorbents: Chitosan hydrogel beads after the removal of copper(II), Chem. Eng. J. 166 (2011) 970–977, https://doi.org/10.1016/j.cej.2010.11.085.
[14] S.P. Zhang, J. Ding, D.Y. Tian, Incorporation of MIL-101 (Fe or Al) into chitosan hydrogel adsorbent for phosphate removal: Performance and mechanism, J. Solid State Chem. 306 (2022) 122709, https://doi.org/10.1016/j.jssc.2021.122709.
[15] H.P. Zeng, S.Q. Sun, K. Xu, W.H. Zhao, R.X. Hao, J. Zhang, D. Li, Iron-loaded magnetic alginate-chitosan double-gel interpenetrated porous beads for phosphate removal from water: Preparation, adsorption behavior and pH stability, React. Funct. Polym. 177 (2022) 105328, https://doi.org/10.1016/j.reactfunctpolym.2022.105328.
[16] S. Pap, C. Kirk, B. Bremner, M.T. Sekulic, L. Shearer, S.W. Gibb, M.A. Taggart, Low-cost chitosan-calcite adsorbent development for potential phosphate removal and recovery from wastewater effluent, Water Res. 173 (2020) 115573, https://doi.org/10.1016/j.watres.2020.115573.
[17] Z. Dou, X. Xie, Chitosan-Montmorillonite-Fe Nanocomposite Hydrogel for Phosphate Recovery and Reuse, ACS ES&T Eng. 3 (2023) 682–689, https://doi.org/10.1021/acsestengg.2c00390.
[18] S.A. Eltaweil, M.A. Omer, G.H. El-Aqapa, N.M. Gaber, F.N. Attia, M.G. El-Subruiti, S.M. Mohy-Eldin, M.E.A. El-Monaem, Chitosan based adsorbents for the removal of phosphate and nitrate: A critical review, Carbohydr. Polym. 274 (2021) 118671, https://doi.org/10.1016/j.carbpol.2021.118671.
[19] C. Bulin, Combination mechanism of the ternary composite based on Fe_3O_4-chitosan-graphene oxide prepared by solvothermal method, Int. J. Biol. Macromol. 231 (2023) 123337, https://doi.org/10.1016/j.ijbiomac.2023.123337.
[20] F.H. Li, J. Jin, Z.Y. Shen, H.S. Ji, M. Yang, Y.M. Yin, Removal and recovery of phosphate and fluoride from water with reusable mesoporous Fe_3O_4@$mSiO_2$@mLDH composites as sorbents, J. Hazard. Mater. 388 (2020) 121734, https://doi.org/10.1016/j.jhazmat.2019.121734.
[21] J.H. Qu, S.Q. Wang, Z.W. Li, S.Q. Wei, F.X. Bi, S.J. Yan, H. Yu, L. Wang, Y. Zhang, Highly efficient recovery of phosphate from water using cerium carbonate hydroxide-decorated magnetic biochar: a slow-release phosphate fertilizer for

agricultural reuse, ACS ES&T Eng. 4 (2024) 3045–3056, https://doi.org/10.1021/acsestengg.4c00407.
[22] T. Bao, M.M. Damtie, Z.M. Yu, Y.W. Liu, J. Jin, K. Wu, C.X. Deng, W. Wei, X.L. Wei, B.J. Ni, Green synthesis of Fe_3O_4@carbon filter media for simultaneous phosphate recovery and nitrogen removal from domestic wastewater in biological aerated filters, ACS Sustain. Chem. Eng. 7 (2019) 16698–16709, https://doi.org/10.1021/acssuschemeng.9b04119.
[23] J. Wan, C. Zhu, J. Hu, T.C. Zhang, D. Richter-Egger, X.N. Feng, A.J. Zhou, T. Tao, Zirconium-loaded magnetic interpenetrating network chitosan/poly(vinyl alcohol) hydrogels for phosphorus recovery from the aquatic environment, Appl. Surf. Sci. 423 (2017) 484–491, https://doi.org/10.1016/j.apsusc.2017.06.201.
[24] Z. Zou, W.H. Tian, X.S. Mao, J.Q. Li, Y.P. Lan, C.Y. Chen, H.Y. Sohn, J.S. Zhang, F. Y. Liu, Synthesis, phase transformation and applications of $CeCO_3OH$: A review, J. Rare Earths 42 (2024) 1403–1420, https://doi.org/10.1016/j.jre.2023.09.003.
[25] A.T. Bah, Z.Y. Shen, J.N. Yan, F.H. Li, Phosphorous recovery from water via batch adsorption enrichment combined with struvite crystallization in a fluidized bed reactor, J. Environ. Chem. Eng. 11 (2023) 110180, https://doi.org/10.1016/j.jece.2023.110180.
[26] F.H. Li, W.H. Wu, R.Y. Li, X.R. Fu, Adsorption of phosphate by acid-modified fly ash and palygorskite in aqueous solution: Experimental and modeling, Appl. Clay Sci. 132 (2016) 343–352, https://doi.org/10.1016/j.clay.2016.06.028.
[27] J.N. Yan, M.Y. Ma, B. Zhao, F.H. Li, Phosphate recovery from wastewater by rapid adsorption-desorption enrichment over UiO-66@melamine sponge composites, J. Water Process Eng. 55 (2023) 104253, https://doi.org/10.1016/j.jwpe.2023.104253.
[28] Z.Y. Shen, J. Jin, J.J. Fu, M. Yang, F.H. Li, Anchoring Al- and/or Mg-oxides to magnetic biochars for Co-uptake of arsenate and fluoride from water, J. Environ. Manag. 293 (2021) 112898, https://doi.org/10.1016/j.jenvman.2021.112898.
[29] F. Hrizi, H. Dhaouadi, F. Touati, Cerium carbonate hydroxide and ceria micro/nanostructures: Synthesis, characterization and electrochemical properties of $CeCO_3OH$, Ceram. Int. 40 (2014) 25–30, https://doi.org/10.1016/j.ceramint.2013.05.098.
[30] W. Li, K.C. Wang, J.J. Huang, X. Liu, D. Fu, J.L. Huang, Q.B. Li, G.W. Zhan, MxOy-ZrO_2 (M = Zn, Co, Cu) solid solutions derived from Schiff base-bridged UiO-66 composites as high-performance catalysts for CO_2 hydrogenation, ACS Appl. Mater. Interfaces 11 (2019) 33263–33272, https://doi.org/10.1021/acsami.9b11547.
[31] J.N. Yan, M.Y. Ma, K.Y. Liu, Y. Bao, F.H. Li, Anchoring NH_2-MIL-101(Fe/Ce) within Melamine sponge boosts rapid adsorption and recovery of phosphate from water, ACS ES&T Eng. 3 (2023) 467–478, https://doi.org/10.1021/acsestengg.2c00324.
[32] J.M. Dorresteijn, R. Conradi, L.D.B. Mandemaker, K. Schnabl, V. Cirriez, A. Welle, D. Curulla-Ferre, F. Meirer, E.T.C. Vogt, B.M. Weckhuysen, Chitosan microsphere-supported catalysts: design, synthesis and optimization for ethylene polymerization, Mater. Adv. 6 (2025) 201–213, https://doi.org/10.1039/d4ma00893f.
[33] Z.M. Mizwari, A.A. Oladipo, E. Yilmaz, Chitosan/metal oxide nanocomposites: synthesis, characterization, and antibacterial activity, Int. J. Polym. Mater. Polym. Biomater. 70 (2021) 383–391, https://doi.org/10.1080/00914037.2020.1725753.
[34] M.N. Afridi, W.H. Lee, J.O. Kim, Effect of phosphate concentration, anions, heavy metals, and organic matter on phosphate adsorption from wastewater using anodized iron oxide nanoflakes, Environ. Res. 171 (2019) 428–436, https://doi.org/10.1016/j.envres.2019.01.055.
[35] J.Y. Liu, L.H. Wan, L. Zhang, Q. Zhou, Effect of pH, ionic strength, and temperature on the phosphate adsorption onto lanthanum-doped activated carbon fiber, J. Colloid Interface Sci. 364 (2011) 490–496, https://doi.org/10.1016/j.jcis.2011.08.067.
[36] M.X. Li, J.Y. Liu, Y.F. Xu, G.R. Qian, Phosphate adsorption on metal oxides and metal hydroxides: A comparative review, Environ. Rev. 24 (2016) 319–332, https://doi.org/10.1139/er-2015-0080.
[37] J.N. Yan, M.Y. Ma, F.H. Li, Revealing the roles of microplastics and dissolved organic matter in phosphorus recovery via struvite crystallization in batch and fluidized-bed reactors, ChemRxiv (2024), https://doi.org/10.26434/chemrxiv-22024-cr26432vg.
[38] N. Pitakteeratham, A. Hafuka, H. Satoh, Y. Watanabe, High efficiency removal of phosphate from water by zirconium sulfate-surfactant micelle mesostructure immobilized on polymer matrix, Water Res. 47 (2013) 3583–3590, https://doi.org/10.1016/j.watres.2013.04.006.
[39] S. Wang, J. Pu, J. Wu, H. Liu, H. Xu, X. Li, H. Wang, SO_4^{2-}/ZrO_2 as a solid acid for the esterification of palmitic acid with methanol: effects of the calcination time and recycle method, ACS Omega 5 (2020) 30139–30147, https://doi.org/10.1021/acsomega.0c04586.
[40] D.S. Tawfik, R.E. Viola, Arsenate replacing phosphate: alternative life chemistries and ion promiscuity, Biochemistry 50 (2011) 1128–1134, https://doi.org/10.1021/bi200002a.
[41] B. Sadeghalvad, N. Khorshidi, A. Azadmehr, M. Sillanpää, Sorption, mechanism, and behavior of sulfate on various adsorbents: A critical review, Chemosphere 263 (2021) 128064, https://doi.org/10.1016/j.chemosphere.2020.128064.
[42] L.P. Weng, W.H. Van Riemsdijk, T. Hiemstra, Humic nanoparticles at the oxide-water interface: interactions with phosphate ion adsorption, Environ. Sci. Technol. 42 (2008) 8747–8752, https://doi.org/10.1021/es801631d.
[43] I. Perassi, L. Borgnino, Adsorption and surface precipitation of phosphate onto $CaCO_3$–montmorillonite: effect of pH, ionic strength and competition with humic acid, Geoderma 232-234 (2014) 600–608, https://doi.org/10.1016/j.geoderma.2014.06.017.
[44] Z. Fu, F. Wu, K. Song, Y. Lin, Y. Bai, Y. Zhu, J.P. Giesy, Competitive interaction between soil-derived humic acid and phosphate on goethite, Appl. Geochem. 36 (2013) 125–131, https://doi.org/10.1016/j.apgeochem.2013.05.015.
[45] M.B. Zahid, X.F. Wang, Y.F. Xia, X.Y. Xu, D.W. Li, F.H. Li, Roles of dissolved organic matters in K-struvite formation in batch and fluidized-bed reactors: a kinetic insight, J. Environ. Chem. Eng. 13 (2025) 118515, https://doi.org/10.1016/j.jece.2025.118515.
[46] R. Nazarian, R.J. Desch, S.W. Thiel, Kinetics and equilibrium adsorption of phosphate on lanthanum oxide supported on activated carbon, Colloids Surf. 624 (2021), https://doi.org/10.1016/j.colsurfa.2021.126813.
[47] M.O. Usman, G. Aturagaba, M. Ntale, G.W. Nyakairu, A review of adsorption techniques for removal of phosphates from wastewater, Water Sci. Technol. 86 (2022) 3113–3132, https://doi.org/10.2166/wst.2022.382.
[48] J.L. Wang, X. Guo, Adsorption isotherm models: Classification, physical meaning, application and solving method, Chemosphere 258 (2020) 127279, https://doi.org/10.1016/j.chemosphere.2020.127279.
[49] K.H. Chu, Revisiting the temkin isotherm: dimensional inconsistency and approximate forms, Ind. Eng. Chem. Res. 60 (2021) 13140–13147, https://doi.org/10.1021/acs.iecr.1c01788.
[50] Y. Zhang, Z.Y. Guo, P.W. Liu, Z. Qiu, V. Gitis, H.J. Feng, Y.F. Li, Y.J. Cai, H. Xiang, H. Li, B. Yu, Hydrogen-bond dominated phosphorus uptake by chitosan-calcium alginate coated melamine foam in ecological floating beds, Chem. Eng. J. 494 (2024) 153303, https://doi.org/10.1016/j.cej.2024.153303.
[51] C. Sudhakar, S. Mukherjee, A.A. Kumar, G. Paramasivam, P.K. Meena, Nonappa, T. Pradeep, Interference of phosphate in adsorption of arsenate and arsenite over confined metastable two-line ferrihydrite and magnetite, J. Phys. Chem. C 125 (2021) 22502–22512, https://doi.org/10.1021/acs.jpcc.1c04317.